One-step fabrication of single-phase hydroxyapatite coatings on Ti-alloy implants by electrostatic spray deposition: From microstructural investigation to in vitro studies

Verónica Müller, Sandra Balvay, Claire Gaillard, Solène Tadier, Laurent Gremillard, Elisabeth Djurado

Version of Record: https://www.sciencedirect.com/science/article/pii/S0257897221009798
Manuscript_d85f77b6ffd5621945168e1eaae27101

One-step fabrication of single-phase hydroxyapatite coatings on Ti-alloy implants by electrostatic spray deposition: From microstructural investigation to *in vitro* studies

Verónica Müller[a,b], Sandra Balvay[b], Claire Gaillard[b], Solène Tadier[b], Laurent Gremillard[b], Elisabeth Djurado[a*]

[a] Univ. Grenoble Alpes, Univ. Savoie Mont Blanc, CNRS, Grenoble INP, LEPMI, 38000 Grenoble, France

[b] Univ Lyon, CNRS, INSA Lyon, UCBL, MATEIS UMR 5510, 69621 Villeurbanne, France

**Corresponding author:* Elisabeth Djurado

E-mail: elisabeth.djurado@lepmi.grenoble-inp.fr, Tel: +33-476826684; Fax: +33-476826777

Abstract:

The intrinsic characteristics of calcium phosphate-based ceramics (composition, crystallinity, morphology) enable them to be successfully used as osseoconductive coatings on load-bearing implants. Among these compounds, hydroxyapatite (HAP) is the leading material owing to its similarity with the mineral component of bone tissue. In this work, electrostatic spray deposition (ESD) using an organic phosphorus precursor was employed as a suitable one-step coating technique that might overcome the drawbacks of the widely used plasma-spraying process related to extremely high processing temperatures, such as unpredictable phase changes of the feedstock, particle release and delamination. The key ESD parameters (type of the solvent(s), total reagent concentration, nominal Ca/P ratio in the precursor solution, solution flow-rate, substrate temperature, and nozzle-to-substrate distance) were systematically studied to tune, precisely, the microstructure and the crystallite size of single-phase HAP coatings on Ti6Al4V substrates. *In vitro* studies with MG-63 osteoblast-like cells were performed during 24 h exposure to selected ESD-derived HAP coatings. All coatings were found to support cell viability. Moreover, the coating properties, *i.e.,* crystallite size and microstructure, played an extremely important role in the behavior of osteoblast-like cells. A higher cellular response was observed when low crystalline HAP coatings were employed.

Keywords: single-phase hydroxyapatite coatings; electrostatic spray deposition; microstructural properties; Ti6Al4V substrate; *in vitro* evaluation; osteoblast-like cells

1. Introduction

Titanium and its alloys (*i.e.*, Ti6Al4V) are commonly used to manufacture load-bearing implants, such as dental and orthopedic implants, due to their excellent mechanical properties (strength and toughness), biocompatibility, and corrosion resistance [1]. Osseoconductive calcium phosphate-based (CaP) coatings are frequently applied to these implants to improve their biological performance [2,3]. The most studied, clinically tested, and used synthetic CaP material is hydroxyapatite ($Ca_{10}(PO_4)_6(OH)_2$, HAP) due to its chemical similarity with the mineral constituent of bone tissue.

Today, the preferentially employed method to deposit CaP coatings onto commercial devices is the atmospheric plasma spraying (APS) technique [4–6]. The advantages of APS lie in its relatively low cost, high deposition rate, and ability to coat large areas [7,8]. However, this technique presents serious concerns associated with the high processing temperature and rapid cooling rate. During the fabrication process, the HAP feedstock transforms, by decomposing into dehydroxylated CaP phases [9,10]. In particular, the impact of molten feedstock hydroxyapatite powder on the metallic surface generates an amorphous calcium phosphate (ACP) phase that might lead to i) an uncontrolled gradient in composition, ii) a poor coating adhesion, and iii) a disparity of bond strengths among the interface coating-metallic substrate [11]. Moreover, APS produces rather thick coatings (50 - 200 µm) that are prone to severe mechanical stresses jeopardizing the success of implants [12,13].

To overcome these drawbacks, alternative processes to deposit thinner HAP-coatings free of secondary phases have been extensively investigated, such as sol-gel deposition [14], electrochemical deposition [15,16], pulsed-laser deposition (PLD) [17], RF magnetron sputtering deposition [18,19] hot isostatic pressing (HIP) [20,21] and micro-arc oxidation [22] Among the

different methods to deposit CaP coatings, the electrostatic spray deposition (ESD) stands as a suitable low-temperature deposition method [23–27] that might help to eliminate some of the drawbacks related to APS.

Based on the principle of electrostatic atomization, ESD is a versatile and low-cost chemical method with a high deposition efficiency that enables the fabrication of coatings with controlled thickness and composition [28–30]. Briefly, the ESD principle is the generation of a spray of micro-sized, charged droplets produced by electrostatic atomization of a precursor solution pumped at a regulated flow-rate through a metallic nozzle (**Fig. S1**). The morphological features of the deposited coatings are determined mainly by the size of the sprayed droplets and their interaction with the heated substrate. According to Gañan-Calvo's equation (**Eq. 1**) [31], the droplets' size at the top of the nozzle (D, µm) can be estimated from the solution's properties (γ, the surface tension [32], ρ, the solvent density [32], and K, the electrical conductivity, ε_0, the vacuum permittivity (8.85×10^{-12} F m^{-1}) and Q, the solution flow-rate.

$$D \sim \left(\frac{\rho \varepsilon_0 Q^3}{\gamma K} \right)^{1/6} \qquad \textbf{(Equation 1)}$$

The size of the droplets impacting the heated substrate relies also on other processing parameters such as the substrate temperature (T), the solution boiling point (b.p.), the nozzle-to-substrate distance (d), and the time of deposition (t) [33,34].

Recently, we have developed a robust one-step process to deposit single-phase nanocrystalline HAP coatings by ESD. The coating fabrication is based on the spray deposition using a solution of triethyl phosphate (TEP) as the P^{5+} precursor and calcium nitrate as the Ca^{2+} precursor [35]. In this recent paper, we have found that the incorporation of TEP as inorganic phosphorus into the deposited coating is strongly conditioned by hydrolysis and evaporation phenomena during the ESD process.

This rigorous study allowed us to understand and propose a mechanism to fabricate crystalline HAP coatings by an innovative bottom-up strategy in a single-step fabrication process. Several processing parameters were explored to find the optimized conditions that enable to reach chemical purity of the deposited coatings. It is well known that even today, the precise control of coatings microstructure remains a technological challenge. The present work is dedicated to an in-depth analysis of the influence of ESD parameters on the morphological properties of single-phase HAP coatings fabricated by this approach. Herein, working under the optimized conditions found in Ref. 35, the effect of selected processing parameters (type of the solvent(s), total reagent concentration, nominal Ca/P ratio in the precursor solution, solution flow-rate, substrate temperature, and nozzle-to-substrate distance) on the HAP coating morphology will be systematically examined. The principal objective of the current work is to highlight the ability of ESD for tuning, precisely, the grain size and microstructure of single-phase HAP coatings. To confirm biocompatibility, osteoblast-like cells (MG-63 cell-line) were cultured on selected HAP coatings and tested for cytocompatibility response. Moreover, after cell-seeding, the morphology of selected coatings was examined to assess their microstructural robustness. The biological performance of HAP is well known to be strongly conditioned by the properties of the coatings, such as crystallinity, phase composition, surface topography, roughness, thickness, and grain size. Thus, as a proof-of-concept, our assays intend to demonstrate the suitability of the ESD technique for manufacturing HAP-coatings with tuned characteristics, designed to modulate their biological response.

2. Material and methods

2.1 ESD as-deposited coatings

Ti6Al4V ELI plates (also referred to as TA6V, Ti64 or grade 23, ACNIS-Titanium; 10 mm in diameter, 2 mm thick) were used as substrates for the coating procedure. Before deposition,

substrates were mirror-polished using a silica suspension (OP-S, 0.25 µm (Struers): H_2O_2 30 wt. % (Hydrogen peroxide, Merck) (3:1)) on a polishing cloth (ChemoMet, Buehler) for 30 min as final polishing-step. Finally, the substrates were cleaned ultrasonically in acetone (15 min.), EtOH (15 min.), and H_2O (10 min.). Working solutions were prepared by mixing calcium nitrate ($Ca(NO_3)_2 \cdot 4H_2O$; 99.95 %, Merck), and triethyl phosphate (TEP, $O=P-(O-CH_2-CH_3)_3$); 99.8%, Sigma-Aldrich), into solvents chosen based on their different physical-chemical properties (**Table 1**). The precursor solutions' conductivity was measured at 25 °C with a CDRV-62 conductimeter. For ESD, these precursor solutions were pumped through a metallic nozzle (tilted-outlet stainless steel needle, 0.6 mm inner diameter and 30 mm length, STERICAN®) at a controlled flow-rate (**Fig. S1**). A potential ranging between 5 and 10 kV, was selected to work in a stable cone-jet mode, characterized by mono-sized droplets in the range of micrometers [36].

In the first part of this work, a systematic study of the effect of ESD deposition parameters, including the type of the solvent(s), total reagent concentration, nominal Ca/P ratio in the solution of precursors, flow-rate (Q), substrate temperature (T), and nozzle-to-substrate distance (d) (**Table 1.I**), on the microstructure of HAP as-deposited coatings was been carried out. For this purpose, a vertical ESD set-up was used to fabricate films. The solutions were delivered through the nozzle by a syringe pump (KD Scientific) with a flow-rate from 0.5 mL h^{-1} to 3 mL h^{-1}. The nozzle-to-substrate distance was varied from 15 mm to 50 mm and the substrate temperature was varied between 325 °C and 400 °C, while the time of deposition was fixed to 1 - 1.5 h. Precursor solutions based on several solvents (methanol (MeOH), MeOH: H_2O (8:2), ethanol (EtOH), EtOH: H_2O (8:2), and butanol (BuOH)) have been evaluated. Droplet sizes at the top of the nozzle were calculated using **Eq. 1** for these different solutions with the density (ρ), surface tension (γ), and b.p., values calculated from a weighted average of the solvents' properties [32] (**Table 1.I.**).

In a second approach, single-phase HAP coatings were selected to assess the biocompatibility of the material and the influence of the coating properties, *i.e.*, microstructure and crystallite size, on their biological performance. To enhance the robustness of the ESD method and to favor the reproducibility of the coatings, a symmetrical multi-substrate holder was designed (**Fig. S1**), allowing to prepare simultaneously four samples. HAP coatings were deposited using a vertical ESD set-up with automatic movement on the X and Y-axes. The transfer from the fixed ESD system devoted to the fabrication of a single coating to the automatic X-Y ESD was ensured by keeping optimized ESD parameters constant and adjusting the deposition time to ensure that the four samples are exposed to the same quantity of precursor solution compared to the fixed system. **Table 1.II** summarizes the ESD parameters for the multiple ESD-deposition processes.

Table 1. ESD processing parameters, nominal Ca/P ratio, estimated physical-chemical properties of the precursor solution, and initial droplet size at the top of the nozzle (D) from **Eq. 1**.

Part I											
Studied parameter	**Type of solvent(s)**	**Ca^{2+} (mM)**	**P^{5+} (mM)**	**Nominal Ca/P ratio**	**b.p. (°C)**	**K (µS cm^{-1})**	**D (µm)**	**t (h)**	**Q (mL h^{-1})**	**T (°C)**	**d (mm)**
Type of solvent(s)	MeOH	15	37.5	0.4	65	850	2.5	1	1.5	350	30
	MeOH: H_2O (8:2)				76	1150	2.1				
	EtOH				78	135	3.4				
	EtOH: H_2O (8:2)				90	560	2.4				
	BuOH				118	13.4	4.1				
Reagent concentration in the precursor solution	EtOH	0.6	3	0.2	78	14.9	5.0	1	1.5	350	30
		3	15			50	4.1				
		7.5	37.5			80	3.8				
		15	75			140	3.4				
Nominal Ca/P ratio of the precursor solution	EtOH	15	18.75	0.8	78	130	3.5	1.5	1.5	350	30
			25	0.6		132	3.5				
			37.5	0.4		135	3.4				
			75	0.2		140	3.4				
Flow-rate (Q)	EtOH	15	18.75	0.8	78	130	2.0	1.5	0.5	350	30
							2.8		1		
							3.5		1.5		
							4.9		3		
Substrate temperature (°C)	EtOH	15	18.75	0.8	78	130	2.8	1.5	1.5	325	30
										350	
										375	

											400	
Nozzle-to-substrate distance (d)	MeOH: H_2O (19:1)	15	10	1.5	70	960	2.4	1.5	1.5	350		15 20 30 50

Part II

Sample code	Type of Solvent(s)	Ca^{2+} (mM)	P^{5+} (mM)	Nominal Ca/P ratio	t (h)	Q (mL h^{-1})	T (°C)	d (mm)	Microstructure of selected HAP coatings		
									Type	Crystallite size (nm)	Thickness
DF	EtOH	0.6	3	0.2	3	1.5	350	30	Thin dense	19 ± 3	70 nm
HC	EtOH	15	18.75	0.8	5	1	350	30	Coral	30 ± 3	26 µm
LC	EtOH	15	75	0.2	5	1	350	30	Coral	16 ± 4	26 µm
RT	MeOH: H_2O (19:1)	15	10	1.5	4.5	1.5	350	15	Reticular	32 ± 4	6 µm

2.2 Microstructural and structural characterizations of the ESD-coatings

The microstructure of all deposited films was examined by scanning electron microscopy (SEM, ZEISS GeminiSEM 500, FEG-SEM), coupled with energy dispersive spectroscopy (EDS, EDAX®), operating at a 6 mm working distance and 5 kV for imaging and a 10 mm working distance and 10 kV for EDS analysis. The particle size of HAP coatings was estimated from the SEM images using an image analysis tool (Image J® SW.). EDS enabled estimations of the Ca/P molar ratio; coatings were analyzed in 5 spots (the center and the four edges of the film) at a 500X magnification. Furthermore, the average thickness of HAP coatings was determined on a cross-sectioned Si-wafer coated under the same conditions as the Ti6Al4V substrates.

The crystallographic structure of selected coatings was determined by a multipurpose X-Pert Pro MPD diffractometer (PANalytical), employing Cu Kα radiation with λ = 1.5419 Å. The diffractogram was collected in Bragg–Brentano geometry across a 2Θ range from 20° to 55°, a 0.026° step width, and ~10 s/step time. Grazing incidence X-ray diffraction (GIXRD) was preferred for the thinnest coatings (DF in **Table 1.II**), to maximize the coating-to-substrate signal ratio [37]. In this case, the measurement was designed with a low fixed incidence angle (0.36°), and a detector scan was performed across a 2θ range from 20° to 55°. An accumulation of 10 scans was collected

on this sample with a measurement time of ~200 min scan^{-1}. The obtained crystalline phases were identified by comparing the PDF (Powder Diffraction File) from the ICDD (International Centre for Diffraction Data). The crystallite size of deposited films was calculated by Scherrer's equation [38,39] using the *(002), (210), (300)*, and *(202)* diffraction peaks. For comparative purposes, a nanocrystalline HAP XRD pattern was simulated based on published cell parameters PDF# 01-074-0565, (Mercury 3.10.3® SW.), and used as an XRD reference of a pure HAP.

Fourier transform infrared spectroscopy (FTIR) from 4000 to 400 cm^{-1} was performed with a resolution of 2 cm^{-1} and 64 scans (ATR mode, Thermo Scientific Nicolet iS50). A commercial HAP powder (SAI, Medical Group) was used to acquire a reference HAP FTIR spectrum.

2.3. Biological characterization

2.3.1 Cell Culture

MG-63 osteoblast-like cells (Cell Culture Passage Number 09; ATCC, Ref CRL-1427) were used to evaluate the *in vitro* response on four selected HAP-coatings (**Table 1.II**). Cells were cultured in 24-well cell culture plates (Corning, NY, USA, ref 3524) with RPMI 1640 medium containing stable L-glutamine and phenol red (Dutscher, France, ref L0498-500) supplemented with 10 % fetal bovine serum (FBS) (Dutscher, ref P040637100) and 5 % antibiotic/antimycotic solution (Dutscher, Ref SV30079.01) as a cell culture medium (CCM) at 37 °C in a humidified atmosphere of 95 % air and 5 % CO_2.

2.3.2. Cell viability of cell-line MG-63

Cell viability (24 h test) was performed on four selected ESD HAP-coatings, named DF, HC, LC, and RT, (**Table 1.II**). Non-coated polished Ti6Al4V discs were used as a control for comparison

with selected samples, to discriminate the influences of the surface morphology and its chemistry (composition and crystallite size). An empty well cell culture plate (plastic) was used as a positive control to validate the assays. Before tests, samples were sterilized by dry heat at 180 °C for 30 min. A cellular suspension at 200.000 cells/mL was prepared using a cell counter (Millipore Scepter Dutscher, ref: 053750) based on the Coulter principle of impedance measurements-particle detection to reliably and accurately count every cell in the sample. After sterilization, the samples were placed separately in the 24-well cell culture plates. 9 samples of each group were used to evaluate cellular response. 50 µL of cellular suspension were deposited at the surface of the materials (10×10^3 cells), and the cell culture plates were incubated for 2 h at 37 °C under a humidified atmosphere (95 % air, 5 % CO_2) to allow cell adhesion. After the addition of 2 mL of cell culture medium (CCM), cells were incubated for 24 h. The cell viability was measured using the PrestoBlue technique (Invitrogen, Carlsbad, CA, USA). This test is based on the resazurin reagent, blue in color and non-fluorescent, which is reduced to resorufin by the mitochondrial metabolic activity of viable cells. Resorufin, pink in color and highly fluorescent, is then used to determine cell viability. After culture, the CCM was discarded and replaced by 1 mL PrestoBlue solution (10 % in cell medium without FBC, antibiotics, and phenol red) in each well. Consequently, the samples were incubated for 1.5 h at 37 °C under a humidified atmosphere of 95 % air, 5 % CO_2. The plates were stirred, and 100 µL of each well was transferred to a 96 black-well plate. The cell fluorescence values were measured at a wavelength of 535 nm using an Infinite Pro 200 fluorimeter (Tecan) with a wavelength of 615 nm for emission. To study the evolution of the coating microstructure after cell-incubation, samples were rinsed several times and subjected to a soft-heat treatment to burn all organic material without compromising the physical-chemical properties of HAP-coatings (375 °C for 2 h). Finally, the coatings were observed by SEM (ZEISS GeminiSEM 500, operating at 5 kV and 6 mm working distance).

2.3.3. Statistical analysis

Measurements to evaluate cell viability were performed in a set of nine samples per microstructure. All fluorescence measurements were performed in triplicate. Results are expressed as means ± standard deviations and are normalized accordingly with the control group response (non-coated polished Ti6Al4V substrate). The *in vitro* cell culture data were compared using an one-way ANOVA test complemented by Tukey-Kramer's test. The significance level was set at $p < 0.05$. Calculations were performed using the OriginPro 8® SW. (OriginLab Corp, Northampton, USA).

3. Results and Discussion

3.1. Microstructural investigation of as-deposited HAP coatings

The ESD technique has drawn considerable attention due to its capacity for preparing ceramic coatings with tunable microstructure [40]. The influence of different ESD parameters, *i.e.*, type of the solvent(s), total reagent concentration, nominal Ca/P ratio in the solution of precursors, flow-rate (Q), substrate temperature (T), and nozzle-to-substrate distance (d) (**Table 1.I**) on the microstructure of as-deposited HAP coatings is investigated in-depth in the following sections.

3.1.1. Influence of the solvent composition

Many processes simultaneously occur during ESD, including the transport and evaporation of droplets from the nozzle to the heated substrate and the impact and spreading of droplets onto the substrate. The physical-chemical properties of the sprayed solutions, affect the kinetics of the abovementioned processes. So, these are key parameters to tailor the coatings' microstructures. Five different solvent compositions of pure MeOH, MeOH: H_2O (8:2), pure EtOH, EtOH: H_2O (8:2), and pure BuOH were selected to examine their effect on the evolution of HAP coatings morphology (**Fig.**

1). All ESD parameters are summarized in **Table 1.I**. The precursors' concentrations were fixed at 15 mM of Ca^{2+} and 37.5 mM of P^{5+} in this section. This large amount of phosphorus precursor used for the preparation of solution (Ca/P molar ratio of 0.4) has the purpose of compensating for TEP evaporation during flight time and ensuring in all cases the deposition of pure HAP coating, as recently reported [35]. In all cases, a crack-free microstructure was obtained. The microstructure of as-deposited coatings from pure MeOH-based solution consists of large precipitates (5-10 µm) made of small particles (310 ± 50 nm diameter), as shown in **Fig. 1a, b**. Indeed, faster evaporation of MeOH (b.p. 65 °C) is expected than of the other solvents during the deposition process. As a consequence, the droplets almost dried completely during flight time, and fast precipitation occurred. Under such circumstances, these dried particles tend to agglomerate during the deposition process due to the electrostatic attraction between charged particles and the more pronounced curvatures of the already coated substrate surface. This phenomenon is known as the preferential landing effect [28,41,42]. The addition of water to pure MeOH (MeOH: H_2O (8:2)) increases the solution b.p. (from 65 to 76 °C) and leads to a slight decrease of the droplet size from 2.5 to 2.1 µm according to **Eq. 1** (since solution conductivity increases from 850 to 1100 µm cm^{-1} (**Table 1.I**), and the surface tension from 0.0247 to 0.0415 N m^{-1} [32]). Consequently, droplets based on MeOH: H_2O (8:2) as a solvent were still liquid and could spread and dry onto the substrate. Both spreading and drying processes, taking place simultaneously at the surface of the substrate, lead to reticular-type coating with an average particle size of (150 ± 60) nm according to image analysis (**Fig. 1c**, **d**). When MeOH: H_2O (8:2) was replaced by ethanolic based solution (EtOH and EtOH: H_2O (8:2)), and then by BuOH, the b.p. of solutions was increased from 76 °C to 78 °C, 90 °C, and 118 °C, respectively, while the droplet size at the top of the nozzle was increased from 2.1 µm to 3.4 µm, 2.4 µm and 4.1 µm, respectively (**Table 1.I**). The final droplet size that impacts the heated substrate also depends on the flight time of the droplets. The smallest droplets of MeOH: H_2O (8:2) solution are expected to be more accelerated in the Taylor cone [36]. Thus, they reach faster the heated-substrate than pure

EtOH, EtOH: H_2O (8:2), and BuOH solutions. As a result, the flight time of droplets based on MeOH: H_2O (8:2) solution was reduced compared to droplets based on pure EtOH, EtOH: H_2O (8:2), and BuOH solutions. In such solutions, a larger amount of solvent evaporated during flight time than in MeOH: H_2O (8:2). A so-called highly porous coral-like microstructure was obtained, for which the particle size was estimated to be (300 ± 50) nm, (380 ± 70) nm, and (350 ± 60) nm for pure EtOH, EtOH: H_2O (8:2), and BuOH solutions, respectively. For sake of clarity, **Fig. 1e-f** shows representative images of such coating morphology using BuOH while SEM views of coating deposited using EtOH-based solutions are displayed in **Fig. S2**. Since the microstructures obtained using BuOH were similar to those obtained from ethanolic-based solutions, the BuOH solvent was not further explored.

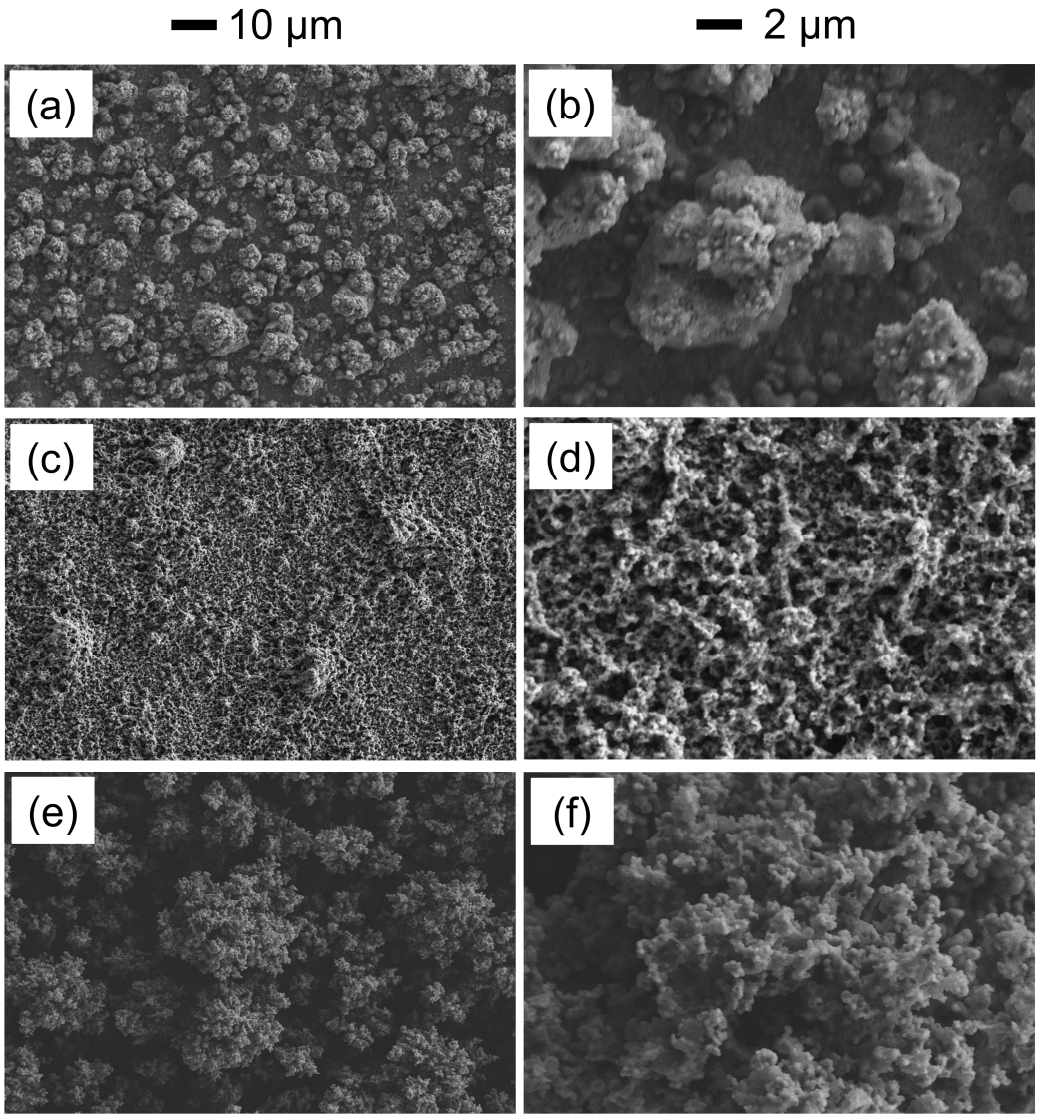

Fig. 1. SEM surface observations of as-deposited coatings obtained with different solvents: MeOH (a, b) MeOH: H_2O (8:2) (c, d), and BuOH (e, f) with a precursor concentration of 15 mM Ca^{2+} and 37.5 mM P^{5+} at 350 °C for a flow-rate of 1.5 mL h^{-1}, a nozzle-to-substrate distance of 30 mm, and a deposition time of 1 h.

3.1.2 Influence of the total reagent concentration

A higher precursor concentration leads to a higher deposition rate in the ESD process, *a priori* offering a reliable and simple way to control the coating thickness [43]. Furthermore, the concentration of precursor is expected to influence the drying and spreading of droplets. To study the minimum reagent dissolution that enabled obtaining a HAP thin-layer free of protrusions, a pure EtOH-based solution containing 15 mM of Ca^{2+} and 75 mM of P^{5+} was subjected to dilutions 1:2,

1:5, and 1:25. ESD deposition parameters are compiled in **Table 1.I**. SEM micrographs of the resulting films are shown in **Fig. 2Ia-d**. From this figure, one can notice that the surface roughness of the coating decreased as the precursor concentration was reduced. Magnified SEM observations are presented in **Fig. S3**. Indeed, the estimated initial droplet size is larger for the diluted solutions than for the more concentrated ones since their conductivity is lower (**Eq. 1**, **Table 1.I**). Thus, a larger spreading of droplets from diluted solutions is expected when impacting the substrate. Additionally, these larger droplets contained a reduced amount of precursor. As a result, HAP precipitation occurred mostly when the droplets impacted the heated-substrate rather than during flight time, leading to smoother surfaces. Once the reagent concentration was low enough (**Fig. 2Id**), the critical supersaturation for HAP precipitation was only reached at this point when massive evaporation of solvent took place. Accordingly, a perfectly flat and thin layer of HAP was obtained for the lowest reagent concentration of 0.6 mM of Ca^{2+} and 3 mM of P^{5+} in EtOH.

3.1.3. Influence of the nominal Ca/P ratio

As recently reported [35], when employing TEP as a P^{5+} source, an excess of precursor must be added to the solution to compensate for its evaporation during the ESD process. The key advantage of using TEP instead of an inorganic phosphorus precursor, *e.g.*, H_3PO_4 [44–46], is its ability to be dissolved in several solvents at high concentration in the presence of a free Ca^{2+} source. Using TEP, Ca/P ratios can be varied willingly without the risk of premature precipitation of undesirable CaP species in the solution of precursors. Furthermore, TEP-based solutions enable a unique chemical strategy to deposit single-phase HAP in a one-step fabrication method. This bottom-up approach suggests the possibility to tune precisely the properties of HAP coatings. In an earlier study [35], a decrease in HAP crystallite size of as-deposited ESD films was observed with decreasing the nominal Ca/P ratio in the precursor solution (the effect was examined by variation of P^{5+}

concentration while the Ca^{2+} content was maintained constant). This tendency might be due to the HAP nucleation that nominates over crystal growth when a large phosphorus concentration is present in the flying droplets [47–49]. This phenomenon is particularly interesting since it could enable the precise control of the dissolution behavior of the HAP coating in a physiological medium. Herein, the influence of the nominal Ca/P ratio on the coating microstructure is investigated. All ESD deposition parameters selected based on our previous work [35], enable fabrication on single-phase HAP coatings and are compiled in **Table 1.I.**

Interestingly, in all cases, a 3D coral-like microstructure was obtained with a similar average grain size of ~300 nm, as shown in **Fig. 2II**, microstructure representative of the whole series. Indeed, the solution conductivity and, therefore, the estimated initial droplet size (**Table 1.I**) were practically identical for all four solutions. The solution conductivity depends on the type of the precursors and the solvent, and it is related to the mobility of ions formed during the dissociation of species in the corresponding solvents [50]. Hence, the solution conductivity is dictated by the presence of the strong electrolytes, Ca^{2+} and NO_3^- [51] rather than by the P^{5+} precursor content. Thus, the variation of TEP concentration, an organic molecule, does not influence the precursor solution conductivity. Furthermore, the pure EtOH solvent (b.p. 78 °C) was submitted to large evaporation during flight time. As a result, even though the crystallite size of HAP is strongly dependent on the Ca/P nominal ratio, the morphology is not affected. Indeed, under these conditions, the sprayed droplets are subjected to a similar preferential landing effect.

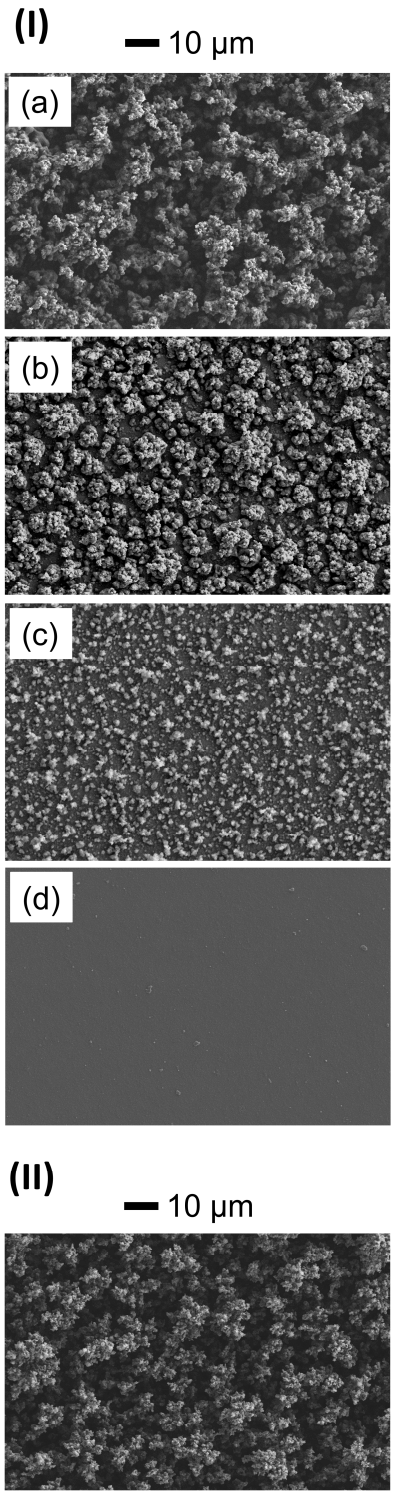

Fig. 2. SEM surface observations of as-deposited coatings obtained at 350 °C for a flow-rate of 1.5 mL h^{-1} a nozzle-to-substrate distance of 30 mm, a pure EtOH-based solution, *for 1 h*. **(I)** 15 mM and Ca^{2+}, and 75 mM P^{5+} (a), 7.5 mM Ca^{2+}, and 37.5 mM P^{5+} (b), 3 mM Ca^{2+}, and 15 mM P^{5+} (c), 0.6 mM Ca^{2+}, and 3 mM P^{5+} (d); *for 1.5 h* **(II)** 15 mM Ca^{2+}, and 25 mM P^{5+}. This morphology is representative of all coatings obtained with different nominal Ca/P ratios.

3.1.4. Influence of the precursor solution flow-rate (Q)

Among the different ESD parameters, the flow-rate of the precursor solution also influences the film morphology because it controls the amount of liquid deposited onto the substrate and the droplet size, according to **Eq. 1**. In this section, coatings were deposited varying the flow-rate from 0.5 mL h^{-1} to 3 mL h^{-1} with pure EtOH based-solution while other processing parameters were kept constant (**Table.1.I**). SEM images are shown in **Fig. 3**. A coral-type morphology was first obtained for a low flow-rate, from 0.5 to 1.5 mL h^{-1}, and then, when this parameter was increased, denser films could be observed. According to **Eq. 1**, the initial droplet size increases when the solution flow-rate is increased. A larger droplet size leads to more limited solvent evaporation during flight. Thus, a larger quantity of solution will spread and dry simultaneously on the heating substrate. Consequently, the coral-like morphology of the coating disappeared when the flow-rate was increased, giving rise to a smooth film. 1 mL h^{-1} is found an optimized flow-rate for depositing a 3D coral-type film homogeneous and highly porous (**Fig. 3a**, **b**).

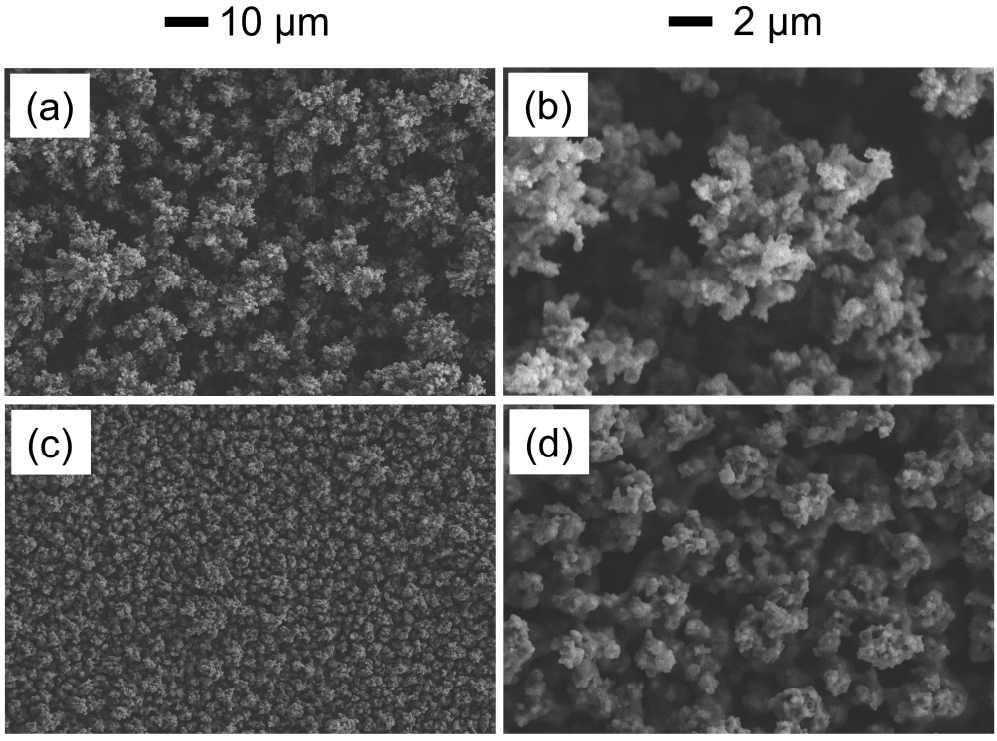

Fig. 3. SEM surface observations of as-deposited coatings obtained with a solution of pure EtOH with a flow-rate of 1 mL h^{-1} (a, b), and 3 mL h^{-1} (c, d) with a precursor concentration of 15 mM Ca^{2+}, and 18.75 mM P^{5+} at 350 °C for a nozzle-to-substrate distance of 30 mm, and a deposition time of 1.5 h.

3.1.5. Influence of the substrate temperature

HAP coatings were deposited at different substrate temperatures, from 325 °C to 400 °C by increments of 25 °C using pure EtOH based-solution with a precursor concentration of 15 mM Ca^{2+}, and 18.75 mM P^{5+}, at a flow-rate, deposition time, and a nozzle-to-substrate of 1.5 mL h^{-1}, 1.5 h and 30 mm, respectively. The minimum temperature of deposition that can be used in this system to produce single-phase HAP coating was 325 °C. This is consistent with the existence of a thermal barrier, due to a competitive process between TEP evaporation and its reactivity to form HAP during electrospraying, as shown in a different study [35]. Furthermore, low boiling point solvents, such as EtOH (**Table 1.I**), should be preferred to prevent massive TEP evaporation [35]. The evolution of coating microstructure versus substrate temperature is shown in **Fig. 4I** for pure EtOH-based solution. When the temperature was increased from 325 °C to 400 °C, the incoming particles became drier and drier. Subsequently, the particle size was much smaller at 400 °C (170 ± 45 nm) than at 325 °C (390 ± 70 nm). When the substrate temperature is increased, the evaporation rate of the droplets during flight time was also increased. This leads to smaller particles impacting the substrate and causes the formation of uneven surfaces sections. The preferential landing effect is more marked, leading to a coral-like, highly porous microstructure. Finally, at T ≥ 375 °C for pure EtOH-based solution, the droplets experienced massive solvent evaporation before reaching the substrate surface. As a result, hollow particles are observed (**Fig. 4e**). This crust-like formation was significant at 375 °C or 400 °C and was due to the heterogeneous concentration profile of the precursors in the flying droplets combined with a fast drying of the remaining solvent when reaching the heated substrate. It

has been demonstrated that the evaporative mass flux of solvent in a droplet that spreads on a heated plate reaches its maximum near the contact line between the droplet and the heated plate [52]. Consequently, the HAP precipitation occurs at the edges of the droplets after reaching critical supersaturation, producing hollow particles at such substrate temperatures. Since these features might decrease the capacity of the coating to withstand mechanical stresses, the substrate temperature was fixed at 350 °C when depositing the selected HAP coatings in the following part of this work.

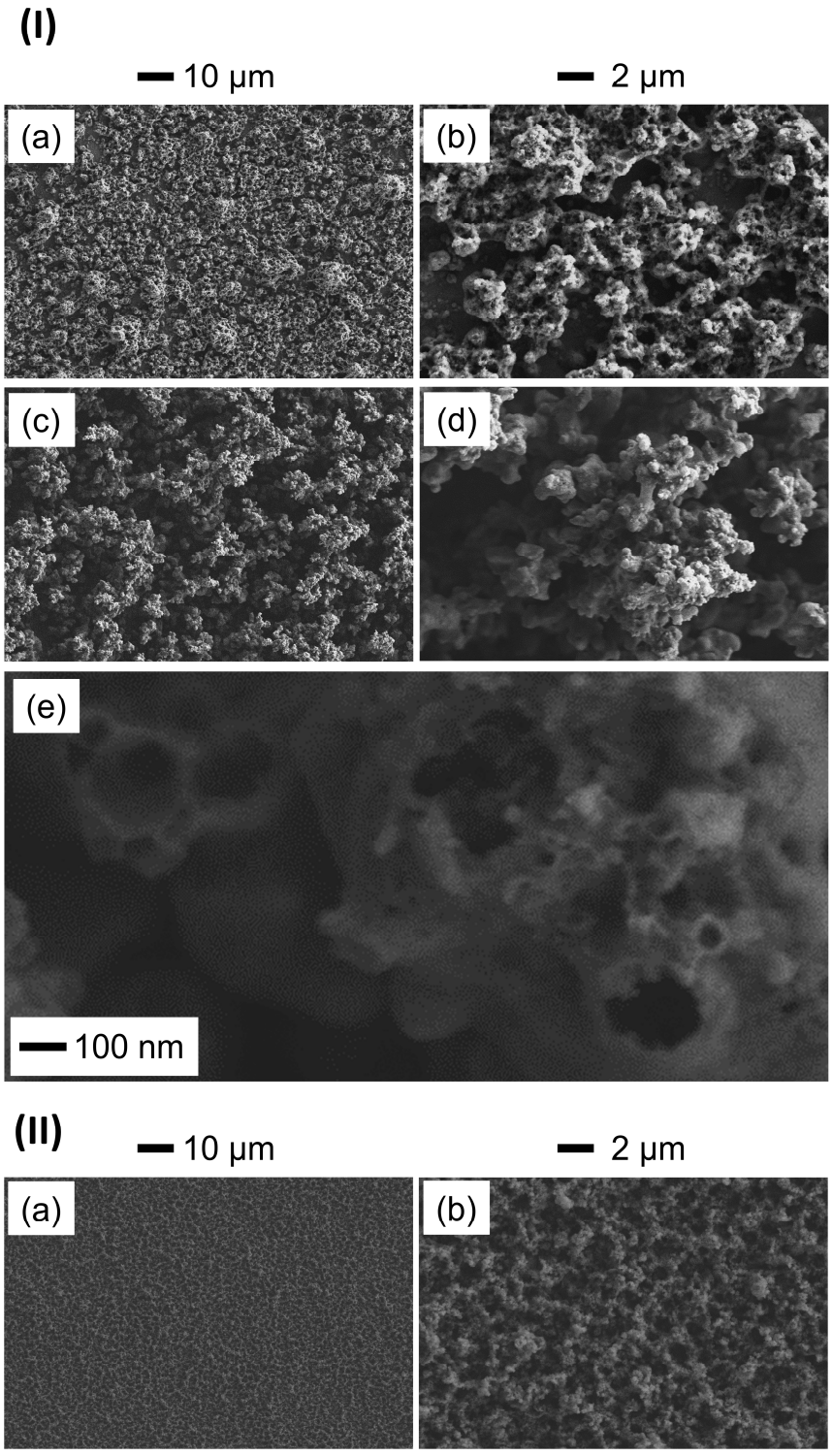

Fig. 4. SEM surface observations of as-deposited coatings for a deposition time of 1.5 h, and a flow-rate of 1.5 mL h^{-1} operating with a solution of **(I)** pure EtOH with a precursor concentration of 15 mM Ca^{2+}, and 18.75 mM P^{5+} at 325 °C (a, b), 350 °C (c, d), zoom view of hollow particles obtained at high substrate temperature ≥ 375 °C (e), and at a nozzle-to-substrate distance of 30 mm; (**II**) MeOH: H_2O (19:1) with a precursor concentration of 15 mM Ca^{2+}, and 10 mM P^{5+} at 350 °C with a nozzle-to-substrate distance of 15 mm (a, b).

3.1.6. Influence of the nozzle-to-substrate distance

In this part, a precursor solution based on MeOH: H_2O (19:1) with concentrations of 15 mM of Ca^{2+} and 10 mM of P^{5+} was preferred to the one previously used in section 3.1.1 (MeOH: H_2O (8:2)). The purpose of using a smaller amount of water is to reduce the conductivity of the precursor solution and, therefore, increase the size of the droplets (**Eq. 1**). A smaller quantity of water also decreases the boiling point of the solution from 83 °C (section 3.1.1) to 70 °C in this new solution. When solvents of low boiling points are used, the TEP evaporation rate is expected to decrease [35]. So, in this section, a TEP content of only 10 mM was used to deposit single-phase HAP coating, as characterized by XRD in the following (section 3.2.1). To examine the effect of spraying distance on the microstructure of HAP films, the depositions were carried out at a nozzle-to-substrate distance of 15, 20, 30, and 50 mm and at a substrate temperature, solution flow-rate, and a deposition time of 350 °C, 1.5 mL h^{-1}, and 1.5 h, respectively. From **Fig. 4II** and **Fig. S4** one can observe that the reticulated morphology was progressively lost while the nozzle-to-substrate distance increased. This parameter affects the flight time of droplets, their evaporation rate, and the size of impacting droplets on the heated substrate. The larger the distance the longer it takes for the droplets to impact the substrate, enabling more solvent to evaporate. As a result, smaller and drier droplets reached the substrate. These particles led to a strong preferential landing effect, producing isolated agglomerates in the surface of substrates, (**Fig. S4**). On the other hand, reticulation occurred at a small distance (15 mm) thanks to the presence of larger droplets containing enough liquid that simultaneously spread and dried when impacting the heated substrate (**Fig. 4II**).One could also expect to regulate the quantity of solution arriving on the heated substrate and, therefore, the microstructure of the coating by adjusting the nozzle-to-substrate distance or the substrate temperature [43]. Indeed, the onset of reticulation is also observed in **Fig. 4a, b**. However, in that case, the liquid droplets spread on the

substrate before drying up. These processes were not entirely simultaneous, and as a consequence, neither it was the formation of reticulation. In other words, we observed a microstructure akin to an agglomerated network. So, the fabrication of reticular coatings requires suitable substrate temperature and nozzle-to-substrate distance to favor simultaneous droplets spreading and drying when impacting the heated substrate.

3.2 Control of microstructure and crystallite size to enhance biological performances of HAP coatings

The chemical composition, the crystallinity, and the microstructure, *e.g.,* surface roughness, thickness of coatings, all impact the biological performances of CaP-based load-bearing implants. The approach developed in Ref. [35] allows the one-step fabrication of single-phase HAP coatings. Since the optimum coating characteristics for commercial devices are still unknown [53], particular attention has been given to correlate the HAP coating morphology with the processing parameters. As a result, controlled microstructures, crack-free and homogenous, ranging from dense to highly porous coatings, were obtained (**Table 1.II**). Moreover, it should be pointed out that the use of a TEP-based solution as a phosphorus precursor allows a bottom-up approach to tune independently the microstructure and the crystallite size of the HAP phase, factors that constitute a decisive advantage of the ESD process, as these two features cannot generally be controlled separately with conventional methods. Indeed, the crystallite size of HAP coatings influences their biological resorption [54,55]. A higher crystallinity decreases bio-resorption since more crystalline phases are known to be more stable [56]. Nonetheless, there is still a debate about the effect of the crystallite size on the behavior of cells interacting with the coating: whereas some studies found that highly crystalline apatite favors the response of cells [19,57], others showed that the adhesion of osteoblast and mesenchymal cells were inhibited at the surface of highly crystalline apatite [58,59]. Here, HAP

ESD-derived samples with tuned properties have been investigated for cytocompatibility of osteoblast-like cells.

3.2.1 Selection of HAP coatings

Four sample types were selected to investigate the biological performance of as-deposited HAP coatings with particular microstructure and grain sizes. These samples consisted of a thin dense film (DF), two coral-like microstructures with low and high crystallinity of HAP (LC and HC, respectively), and a reticular-type film (RT) (**Table 1.II**). Besides, to enhance the robustness of the ESD method and the biological characterization, a scale-up process was performed, allowing to obtain four samples simultaneously (see section 2.1). In all cases, deposition time was increased to ensure the exposure of the Ti6Al4V substrate to the same quantity of precursor solution as in the ESD-fixed system. The parameters used to obtain the four types of samples are summarized in **Table 1.II**.

The selected HAP coatings differ qualitatively in crystallite size, microstructure, *i.e.*, porosity, roughness, and thickness (**Fig. 5I, II**).

3.2.2. Physicochemical characterization of selected HAP coatings

SEM observations of coatings deposited using the scale-up process are shown in **Fig. 5I** and confirmed that the obtained microstructures were comparable with the optimized ones in previous sections using the ESD process for one coating. EDS analysis revealed a Ca/P ratio of 1.8 - 1.9 for all samples. As shown previously [35], the EDS technique always tends to overestimate the Ca/P value on ESD coatings, probably as the result of preferential evaporation of phosphorus atoms under the

electron beam. The observed Ca/P value of 1.8 - 1.9 by EDS corresponded to a Ca/P ratio of 1.6 as measured by ICP, which corresponds to single-phase HAP coatings. DF, HC, and LC samples were obtained using pure EtOH-based solutions. When the total reagent concentration was lowest, denser thin films (DF), ~70 nm thick were obtained, as discussed in section 3.1.2 (**Fig. 5Ia** and **Fig. 5IIa**). **Fig. 5Ib** and **Fig. 5Ic** show SEM observations of highly porous 3D coral-like microstructure (HC and LC, respectively), both ~26 µm thick (**Fig. 5IIb** and **Fig. 5IIc**). The mean particle size was estimated to be ~300 nm from image analysis. Finally, reticular-type (RT), ~6 µm thick, was obtained using MeOH: H_2O (19:1) based-solution with an estimated particle size of ~250 nm (**Fig. 5Id** and **Fig. 5IId**).

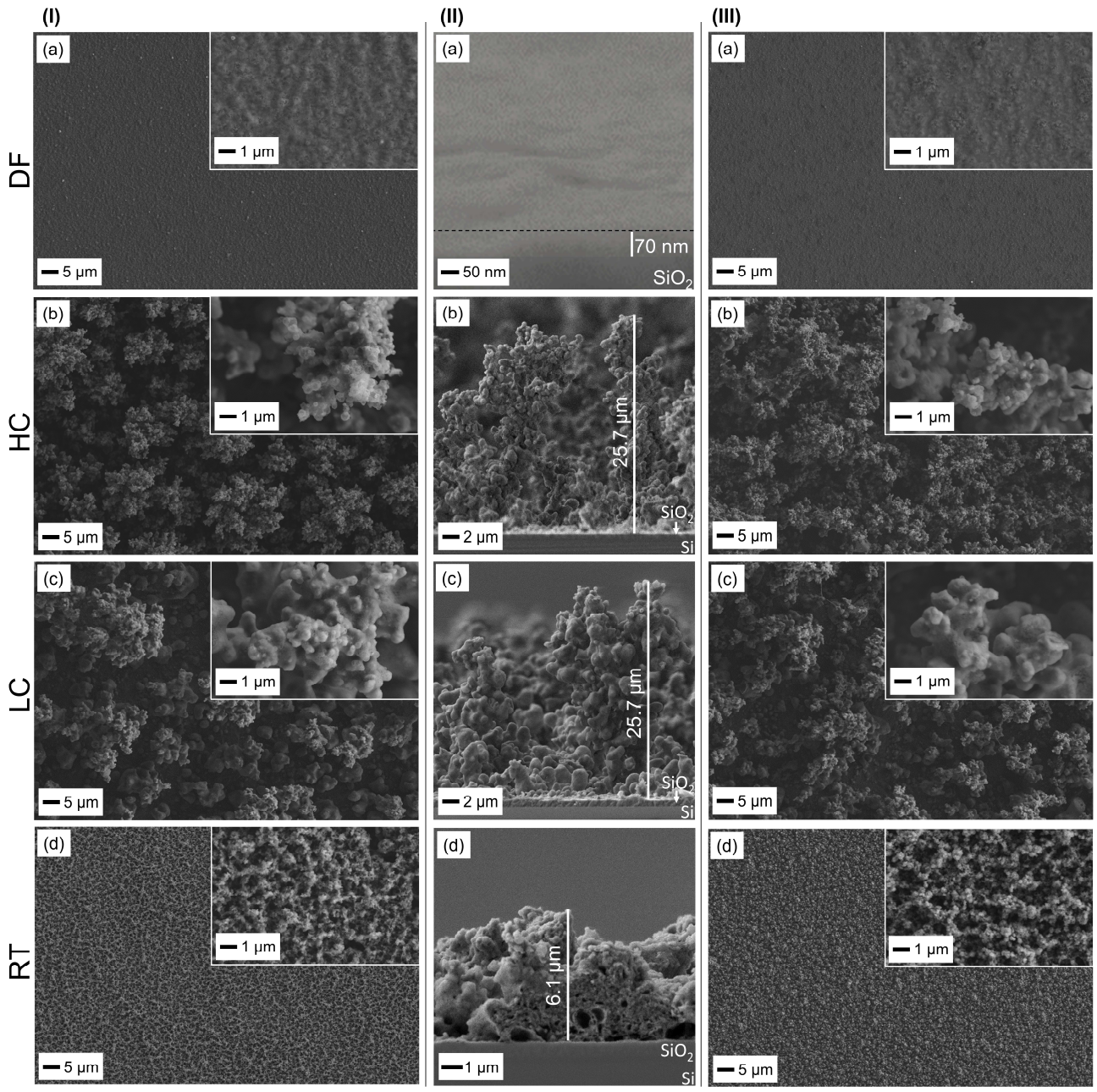

Fig. 5. SEM images of as-deposited HAP selected coatings for biological characterizations: **(I)** surface of (a) DF, (b) HC, (c) LC, (d) RT; **(II)** cross-section on top of Si wafer of (a) DF, (b) HC, (c) LC, (d) RT; **(III)** surface of (a) DF, (b) HC, (c) LC, (d) RT after cell-seeding. On the cross-sectioned view of the DF sample, the dashed line is added as a guide to the eyes to highlight the top of the HAP thin layer. ESD parameters are reported in **Table 1.II**.

Structural properties of selected HAP coatings were characterized by XRD and FTIR. The X-ray diffractograms of coatings are shown in **Fig. 6a**. In all cases, only peaks corresponding to the Ti6Al4V substrate and HAP were detected. The HAP phase was indexed to a hexagonal unit cell with a *P6₃/m* space group (#176) according to PDF# 01-074-0565. The Ti6Al4V substrate was identified to a hexagonal unit cell with a *P6₃/mmc* space group, #194, PDF# 04-002-8708. Additionally, a broadening of HAP peaks can be observed (**Fig. 6a**) for the samples DF and LC, obtained using a low Ca/P nominal ratio (0.2) in an EtOH-based solution (**Table 1.II**) which is coherent with a decrease in the crystallite size. Indeed, the calculated average crystallite size for samples DF and LC was (19 ± 3) nm and (16 ± 4) nm, respectively, contrasted with (30 ± 3) nm and (32 ± 4) nm for samples HC and RT. In this system, the variation of grain size, already reported in our previous work [35], is likely to occur due to the use of a low nominal Ca/P ratio in the precursor solution, which favors the HAP nucleation over its crystal growth during the fabrication process. Certainly, even though the total precursor concentration to deposited DF and LC samples is different, the HAP crystallite size seems to be dictated by the Ca/P nominal ratio. Consequently, the formed HAP crystals had similar crystallite sizes for DF and LC samples. Once again, this feature of the ESD technique is of great relevance since it opens the door to precise tailoring of the HAP resorption rate [54,55]. FTIR spectra (**Fig. 6b**) show the characteristic features of the PO_4^{3-} groups in the hydroxyapatite structure. The band between 560-600 cm^{-1} corresponding to ν_4 PO_4^{3-} bending-mode, triply degenerated. The peak at 960 cm^{-1} is related to ν_1 PO_4^{3-} symmetric stretching-mode, non-degenerated. The broadband between 1020-1120 cm^{-1} corresponds to ν_3 PO_4^{3-} asymmetric stretching-mode, triply degenerated. Lastly, -OH signatures are observed at 630 cm^{-1} assigned to ν_L librational-mode and a narrow peak at 3568 cm^{-1} corresponds to the ν_s stretching-mode [60]. Moreover, additional bands associated with CO_3^{2-} incorporated into the structure of apatite are observed in the IR spectrum. These peaks, at 870 (ν_2 CO_3^{2-}), and 1410-1455 cm^{-1} (ν_3 CO_3^{2-}) [61], are the spectral signature of the mostly b-type substituted carbonate HAP, where CO_3^{2-} occupies PO_4^{3-} lattice sites in

the apatite structure [62,63]. This carbonate content comes mainly from the decomposition during the ESD process of the organic solvent and, in the minority, of TEP [35,45].

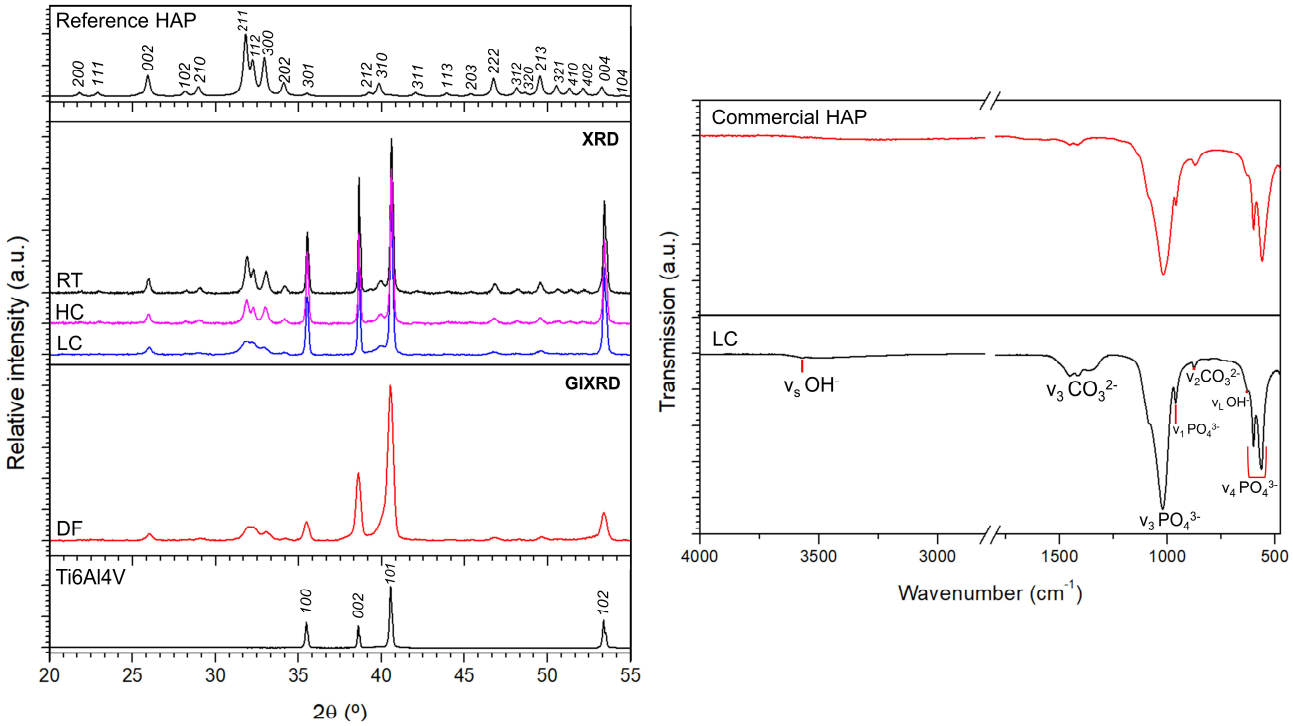

Fig. 6. (a) XRD patterns of selected as-deposited HAP coatings; samples LC, HC, and RT were measured using Bragg–Brentano geometry while grazing incidence X-ray diffraction (GIXRD) was used to characterize the thinner DF sample. (b) FTIR analysis of LC sample. For the sake of clarity, only one FTIR spectrum is shown as it is representative of all spectra obtained for HC, RT, and DF coatings.

3.2.3 Cell viability of MG-63 osteoblast-like cells and microstructural study of HAP coatings after cell-seeding

In this section, the cytocompatibility of HAP ESD-derived coatings and the extent to which their microstructure (morphology, roughness, and thickness) and crystallite size might affect the biological performances are studied. **Fig. 7** shows that all selected coatings supported the cell viability of the MG-63 cell line after 24 h culturing. DF, LC, and RT samples displayed a similar response as the one of the control Ti6Al4V disc. Clear lower cell viability ($^{**}p < 0.001$ compared to

Ti6Al4V reference) is detected for the HC samples. A striking difference is observed in the cell viability ($^{*}p < 0.01$) for samples with coral-like microstructure, where HC samples showed lower cellular viability than the LC samples, which may confirm that grain size would play an essential role in cell behavior for a similar morphology, at least in the earlier implantation period. Indeed, it has been reported [56] that cellular response could be compromised by the high crystallinity of CaP ceramics which might indicate that more soluble phases in the coatings would be more desirable and would result in a stable interface with the physiological environment. Although this is still under debate. Indeed, it has been reported that a too high dissolution rate might lead to less stable surfaces for cell adhesion and spreading [64,65]. This observation agrees with our results. In the case of the RT morphology characterized by large crystallite size (32 nm), an unexpectedly high response of cell viability is measured compared with sample HC ($^{**}p < 0.001$). A possible reason for this behavior would be that a certain wettability of HAP coatings is more efficient for the cell viability and would be larger for RT than for the coral type. Similar cell viability is observed for the very thin and smooth DF HAP coatings with one of the rough LC specimens, both characterized by a similar HAP crystallite size but different thicknesses and surface roughness. In these conditions, it appears that neither coating thickness nor roughness influence MG-63 cellular behavior at 24 h. Nonetheless, additional experiments, such as cell attachment and cell morphology, would be needed to support our claim.

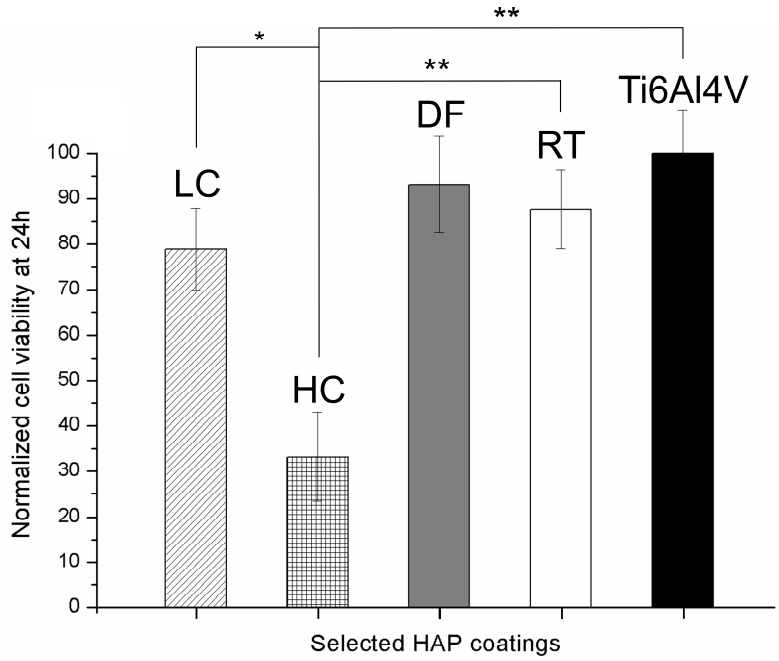

Fig. 7. Cell viability at 24 h of osteoblast-like cells (MG-63 cell-line) for selected HAP coatings, bare and mirror-polished Ti6Al4V substrate were used as the control group. Values represent means ± SD (n = 9). * indicates $p < 0.01$, and ** indicates $p < 0.001$.

SEM images of the samples after post-seeding are shown in **Fig. 5.III**. The surface after cell exposure of all coatings displayed almost imperceptible changes. A dense layer for DF, a coral-like microstructure for HC and LC samples, and the reticulated morphology for RT are retrieved. No dissolution was detected in the HC or RT samples as expected in coatings characterized by a larger crystallite size. In the case of the LC sample, at higher magnification (**Fig. 5.IIIc**), some coating dissolution can be noticed (compared with **Fig. 5.Ic**). A larger SEM micrograph of the LC sample is added in **Fig. S5** for clarification. The smooth surface of DF samples did not allow to detect any clear dissolution features, but a similar behavior could be expected since the DF sample presents a comparable grain size to the LC one. However, one could also hypothesize that the coral-like sample might be subjected to an accelerated dissolution during the test due to its high specific surface area and porosity. Thus, the surface reactivity of the LC sample could be expected to occur more than the

one of the DF layer. Once again, further investigation is required to decorrelate biological performance *vs.* coating properties.

To conclude, cell viability tests are fundamental to assess the biocompatibility of these coatings with unique morphologies. These tests are the cornerstone for evaluating their potential toxic effect and optimizing future efforts. In this study, the cell viability of HAP ESD-derived samples with tuned properties has been studied at 24 h with two principal objectives: i) examine the viability of HAP ESD-derived coatings, ii) highlight the strong relationship between the characteristics of the HAP coatings, *i.e.,* microstructure and crystallite size with their biological performance. We must emphasize that ESD is a suitable alternative to coat HAP since all samples presented a good *in vitro* response. Moreover, we have demonstrated that the coating properties play a significant role in the behavior of the MG-63 osteoblast-like cells. Studies such as cell morphology, attachment, proliferation, and mineralization response are in progress to better understand cell response versus HAP ESD-coatings.

4. Conclusion

The ESD process by using a TEP precursor constitutes a straightforward alternative to the plasma spraying technique to produce single-phase HAP coatings in one step with tunable morphologies and crystallite size. An in-depth analysis of the influence of ESD parameters on coating microstructure was performed. Various morphologies, ranging from thin dense films to highly porous reticular and coral-like topography, were deposited by varying the ESD key process parameters, such as the type of the solvent(s), the total reagent concentration, nominal Ca/P ratio in the precursor solution, solution flow-rate, substrate temperature, and nozzle-to-substrate distance. Our results enabled us to independently tune the microstructure and the HAP crystallite size while ensuring the chemical and phase purity of the coating. The biological response of selected coatings was analyzed by cell culture

tests of MG-63 osteoblast-like cells during 24 h culturing, showing that all HAP ESD-derived coatings are biocompatible. A strong correlation between the properties of the ESD HAP coatings and their biological performance was observed. At 24 h, higher cell viability was observed for coatings characterized by a smaller crystallite size.

5. Acknowledgments

The authors are grateful to Thierry Encinas for XRD support and Frédéric Charlot for SEM and EDS analyses in CMTC (Grenoble INP, France), and the financial support of the French National Agency of Research (DECaP Project ANR-17-CE19-0004).

6. References

[1] A. Civantos, E. Martínez-Campos, V. Ramos, C. Elvira, A. Gallardo, A. Abarrategi, Titanium Coatings and Surface Modifications: Toward Clinically Useful Bioactive Implants, ACS Biomater. Sci. Eng. 3 (2017) 1245–1261. https://doi.org/10.1021/acsbiomaterials.6b00604.

[2] J. Huang, S.M. Best, W. Bonfield, R.A. Brooks, N. Rushton, S.N. Jayasinghe, M.J. Edirisinghe, In vitro assessment of the biological response to nano-sized hydroxyapatite, J. Mater. Sci. Mater. Med. 15 (2004) 441–445. https://doi.org/10.1023/B:JMSM.0000021117.67205.cf.

[3] M. Metikoš-Huković, E. Tkalacec, A. Kwokal, J. Piljac, An in vitro study of Ti and Ti-alloys coated with sol-gel derived hydroxyapatite coatings, Surf. Coatings Technol. 165 (2003) 40–50. https://doi.org/10.1016/S0257-8972(02)00732-6.

[4] D. Ke, A.A. Vu, A. Bandyopadhyay, S. Bose, Compositionally graded doped hydroxyapatite coating on titanium using laser and plasma spray deposition for bone implants, Acta Biomater. 84 (2019) 414–423. https://doi.org/10.1016/j.actbio.2018.11.041.

[5] Y.L. Gao, Y. Liu, X.Y. Song, Plasma-Sprayed Hydroxyapatite Coating for Improved Corrosion Resistance and Bioactivity of Magnesium Alloy, J. Therm. Spray Technol. 27 (2018) 1381–1387. https://doi.org/10.1007/s11666-018-0760-9.

[6] I. Demnati, D. Grossin, C. Combes, C. Rey, Plasma-Sprayed apatite Coatings: Review of physical-chemical characteristics and their biological consequences, J. Med. Biol. Eng. 34 (2014) 1–7. https://doi.org/10.5405/jmbe.1459.

[7] A.A. Campbell, Bioceramics for implant coatings, Mater. Today. 6 (2003) 26–30. https://doi.org/10.1016/S1369-7021(03)01128-3.

[8] A. Nasar, Hydroxyapatite and its coatings in dental implants, in: Appl. Nanocomposite Mater. Dent., Elsevier, 2019: pp. 145–160. https://doi.org/10.1016/B978-0-12-813742-0.00008-0.

[9] V. Pálka, E. Poštrková, H.K. Koerten, Some characteristics of hydroxylapatite powder particles after plasma spraying, Biomaterials. 19 (1998) 1763–1772. https://doi.org/10.1016/S0142-9612(98)00087-8.

[10] O. Graßmann, R.B. Heimann, Compositional and microstructural changes of engineered plasma-sprayed hydroxyapatite coatings on Ti6Al4V substrates during incubation in protein-free simulated body fluid, J. Biomed. Mater. Res. 53 (2000) 685–693. https://doi.org/10.1002/1097-4636(2000)53:6<685::AID-JBM11>3.0.CO;2-B.

[11] E. Mohseni, E. Zalnezhad, A.R. Bushroa, Comparative investigation on the adhesion of hydroxyapatite coating on Ti-6Al-4V implant: A review paper, Int. J. Adhes. Adhes. 48

(2014) 238–257. https://doi.org/10.1016/j.ijadhadh.2013.09.030.

[12] A.K. Lynn, D.L. DuQuesnay, Hydroxyapatite-coated Ti–6Al–4V. Part 1: the effect of coating thickness on mechanical fatigue behaviour, Biomaterials. 23 (2002) 1937–1946. https://doi.org/10.1016/s0142-9612(01)00321-0.

[13] C.Y. Yang, B.C. Wang, T.M. Lee, E. Chang, G.L. Chang, Intramedullary implant of plasma-sprayed hydroxyapatite coating: An interface study, J. Biomed. Mater. Res. 36 (1997) 39–48. https://doi.org/10.1002/(SICI)1097-4636(199707)36:1<39::AID-JBM5>3.0.CO;2-M.

[14] C. Domínguez-Trujillo, E. Peón, E. Chicardi, H. Pérez, J.A. Rodríguez-Ortiz, J.J. Pavón, J. García-Couce, J.C. Galván, F. García-Moreno, Y. Torres, Sol-gel deposition of hydroxyapatite coatings on porous titanium for biomedical applications, Surf. Coatings Technol. 333 (2018) 158–162. https://doi.org/10.1016/j.surfcoat.2017.10.079.

[15] M. Łukaszewska-Kuska, P. Krawczyk, A. Martyla, W. Hędzelek, B. Dorocka-Bobkowska, Hydroxyapatite coating on titanium endosseous implants for improved osseointegration: Physical and chemical considerations, Adv. Clin. Exp. Med. 27 (2018) 1055–1059. https://doi.org/10.17219/acem/69084.

[16] L. Dejob, B. Toury, S. Tadier, L. Grémillard, C. Gaillard, V. Salles, Electrospinning of in situ synthesized silica-based and calcium phosphate bioceramics for applications in bone tissue engineering: A review, Acta Biomater. 123 (2021) 123–153. https://doi.org/10.1016/j.actbio.2020.12.032.

[17] G.C. Gomes, F.F. Borghi, R.O. Ospina, E.O. López, F.O. Borges, A. Mello, Nd:YAG (532 nm) pulsed laser deposition produces crystalline hydroxyapatite thin coatings at room temperature, Surf. Coatings Technol. 329 (2017) 174–183. https://doi.org/10.1016/j.surfcoat.2017.09.008.

[18] V. Nelea, C. Morosanu, M. Iliescu, I.N. Mihailescu, Microstructure and mechanical properties of hydroxyapatite thin films grown by RF magnetron sputtering, Surf. Coatings Technol. 173 (2003) 315–322. https://doi.org/10.1016/S0257-8972(03)00729-1.

[19] R.A. Surmenev, A review of plasma-assisted methods for calcium phosphate-based coatings fabrication, Surf. Coatings Technol. 206 (2012) 2035–2056. https://doi.org/10.1016/j.surfcoat.2011.11.002.

[20] M.A. Auger, B. Savoini, A. Muñoz, T. Leguey, M.A. Monge, R. Pareja, J. Victoria, Mechanical characteristics of porous hydroxyapatite/oxide composites produced by post-sintering hot isostatic pressing, Ceram. Int. 35 (2009) 2373–2380. https://doi.org/10.1016/j.ceramint.2009.01.016.

[21] M. Buchi Suresh, P. Biswas, V. Mahender, R. Johnson, Comparative evaluation of electrical conductivity of hydroxyapatite ceramics densified through ramp and hold, spark plasma and post sinter Hot Isostatic Pressing routes, Mater. Sci. Eng. C. 70 (2017) 364–370. https://doi.org/10.1016/j.msec.2016.09.023.

[22] X. Yang, S. Yu, W. Li, Preparation of bioceramic films containing hydroxyapatites on Ti-6Al-4V alloy surfaces by the micro-arc oxidation technique, Mater. Res. Bull. 44 (2009) 947–949. https://doi.org/10.1016/j.materresbull.2008.09.048.

[23] S.C.G. Leeuwenburgh, J.G.C. Wolke, M.C. Siebers, J. Schoonman, J.A. Jansen, In vitro and in vivo reactivity of porous, electrosprayed calcium phosphate coatings, Biomaterials. 27 (2006) 3368–3378. https://doi.org/10.1016/j.biomaterials.2006.01.052.

[24] W.H. Lee, Y.H. Kim, N.H. Oh, Y.W. Cheon, Y.J. Cho, C.M. Lee, K.B. Kim, N.S. Lee, A Study of Hydroxyapatite Coating on Porous Ti Compact by Electrostatic Spray Deposition, Solid State Phenom. 124–126 (2007) 1789–1792.

https://doi.org/10.4028/www.scientific.net/SSP.124-126.1789.

[25] W. Jiang, L. Sun, G. Nyandoto, A.P. Malshe, Electrostatic spray deposition of nanostructured hydroxyapatite coating for biomedical applications, J. Manuf. Sci. Eng. Trans. ASME. 130 (2008) 0210011–0210017. https://doi.org/10.1115/1.2816016.

[26] M. Iafisco, R. Bosco, S.C.G. Leeuwenburgh, J.J.J.P. Van Den Beucken, J.A. Jansen, M. Prat, N. Roveri, Electrostatic spray deposition of biomimetic nanocrystalline apatite coatings onto titanium, Adv. Eng. Mater. 14 (2012) 13–20. https://doi.org/10.1002/adem.201180062.

[27] T. Mokabber, Q. Zhou, A.I. Vakis, P. van Rijn, Y.T. Pei, Mechanical and biological properties of electrodeposited calcium phosphate coatings, Mater. Sci. Eng. C. 100 (2019) 475–484. https://doi.org/10.1016/j.msec.2019.03.020.

[28] D. Marinha, L. Dessemond, E. Djurado, Comprehensive Review of Current Developments in IT-SOFCs, Curr. Inorg. Chem. 3 (2013) 2–22. https://doi.org/10.2174/1877944111303010003.

[29] V. Müller, M. Jobbagy, E. Djurado, Coupling sol-gel with electrospray deposition: Towards nanotextured bioactive glass coatings, J. Eur. Ceram. Soc. 41 (2021) 7288–7300. https://doi.org/10.1016/j.jeurceramsoc.2021.07.041.

[30] A. Jaworek, A.T. Sobczyk, Electrospraying route to nanotechnology: An overview, J. Electrostat. 66 (2008) 197–219. https://doi.org/10.1016/j.elstat.2007.10.001.

[31] A.M. Gañán-Calvo, J. Dávila, A. Barrero, Current and droplet size in the electrospraying of liquids. Scaling laws, J. Aerosol Sci. 28 (1997) 249–275. https://doi.org/10.1016/S0021-8502(96)00433-8.

[32] D.R. Lide, CRC Handbook of Chemistry and Physics, CRC Press, 2016. https://doi.org/10.1201/9781315380476.

[33] J.F. de la Mora, I.G. Loscertales, The current emitted by highly conducting Taylor cones, J. Fluid Mech. 260 (1994) 155–184. https://doi.org/10.1017/S0022112094003472.

[34] O. Wilhelm, L. Mädler, S.E. Pratsinis, Electrospray evaporation and deposition, J. Aerosol Sci. 34 (2003) 815–836. https://doi.org/10.1016/S0021-8502(03)00034-X.

[35] V. Müller, T. Pagnier, S. Tadier, L. Gremillard, M. Jobbagy, E. Djurado, Design of advanced one-step hydroxyapatite coatings for biomedical applications using the electrostatic spray deposition, Appl. Surf. Sci. 541 (2021) 148462. https://doi.org/10.1016/j.apsusc.2020.148462.

[36] G. Taylor, Disintegration of water drops in an electric field, Proc. R. Soc. London. Ser. A. Math. Phys. Sci. 280 (1964) 383–397. https://doi.org/10.1098/rspa.1964.0151.

[37] J. Als-Nielsen, D. Jacquemain, K. Kjaer, F. Leveiller, M. Lahav, L. Leiserowitz, Principles and applications of grazing incidence X-ray and neutron scattering from ordered molecular monolayers at the air-water interface, Phys. Rep. 246 (1994) 251–313. https://doi.org/10.1016/0370-1573(94)90046-9.

[38] C.R. Hubbards, C.S. Barrett, P.K. Predecki, D.E. Leyden, Advances in X-ray Analysis, Vol. 26, 1982.

[39] S.N. Danilchenko, O.G. Kukharenko, C. Moseke, I.Y. Protsenko, L.F. Sukhodub, B. Sulkio-Cleff, Determination of the bone mineral crystallite size and lattice strain from diffraction line broadening, Cryst. Res. Technol. 37 (2002) 1234–1240. https://doi.org/10.1002/1521-4079(200211)37:11<1234::AID-CRAT1234>3.0.CO;2-X.

[40] D. Marinha, C. Rossignol, E. Djurado, Influence of electrospraying parameters on the microstructure of La0.6Sr0.4Co0.2F0.8O 3-δ films for SOFCs, J. Solid State Chem. 182 (2009) 1742–1748. https://doi.org/10.1016/j.jssc.2009.04.018.

[41] A. Lintanf, A. Mantoux, E. Blanquet, E. Djurado, Elaboration of Ta2O5 thin films using electrostatic spray deposition for microelectronic applications, J. Phys. Chem. C. 111 (2007) 5708–5714. https://doi.org/10.1021/jp0676585.

[42] C.H. Chen, M.H.J. Emond, E.M. Kelder, B. Meester, J. Schoonman, Electrostatic sol-spray deposition of nanostructured ceramic thin films, J. Aerosol Sci. 30 (1999) 959–967. https://doi.org/10.1016/S0021-8502(98)00075-5.

[43] R. Neagu, D. Perednis, A. Princivalle, E. Djurado, Influence of the process parameters on the ESD synthesis of thin film YSZ electrolytes, Solid State Ionics. 177 (2006) 1981–1984. https://doi.org/10.1016/j.ssi.2006.05.052.

[44] S. Leeuwenburgh, J. Wolke, J. Schoonman, J. Jansen, Electrostatic spray deposition (ESD) of calcium phosphate coatings, J. Biomed. Mater. Res. - Part A. 66 (2003) 330–334. https://doi.org/10.1002/jbm.a.10590.

[45] S.C.G. Leeuwenburgh, J.G.C. Wolke, J. Schoonman, J.A. Jansen, Influence of precursor solution parameters on chemical properties of calcium phosphate coatings prepared using Electrostatic Spray Deposition (ESD), Biomaterials. 25 (2004) 641–649. https://doi.org/10.1016/S0142-9612(03)00575-1.

[46] S.C.G. Leeuwenburgh, J.G.C. Wolke, L. Lommen, T. Pooters, J. Schoonman, J.A. Jansen, Mechanical properties of porous, electrosprayed calcium phosphate coatings, J. Biomed. Mater. Res. Part A. 79 (2006) 963–73. https://doi.org/10.1002/jbm.a.

[47] E.K. Titaeva, V.B. Fedoseev, Specific features of crystallization of supersaturated solution in femtoliter-volume systems, Crystallogr. Reports. 59 (2014) 437–441. https://doi.org/10.1134/S1063774514030195.

[48] G. Galster, K.F. Nielsen, Crystal Growth From Solution., Eur. Sp. Agency, (Special Publ. ESA SP. (1984) 189–191. https://doi.org/10.1098/rspa.1949.0060.

[49] I.H. Leubner, A balanced nucleation and growth model for controlled precipitations, J. Dispers. Sci. Technol. 22 (2001) 125–138. https://doi.org/10.1081/DIS-100102688.

[50] L. Onsager, R.M. Fuoss, Irreversible processes in electrolytes. Diffusion, conductance, and viscous flow in arbitrary mixtures of strong electrolytes, J. Phys. Chem. 36 (1932) 2689–2778. https://doi.org/10.1021/j150341a001.

[51] R.K. Srour, L.M. McDonald, Ionic conductivity of selected 2:1 electrolytes in dilute solutions of mixed aqueous-organic solvents at 298.15 K, J. Chem. Eng. Data. 53 (2008) 335–342. https://doi.org/10.1021/je700313j.

[52] C. Sodtke, V.S. Ajaev, P. Stephan, Dynamics of volatile liquid droplets on heated surfaces: Theory versus experiment, J. Fluid Mech. 610 (2008) 343–362. https://doi.org/10.1017/S0022112008002759.

[53] R.A. Surmenev, M.A. Surmeneva, A critical review of decades of research on calcium phosphate–based coatings: How far are we from their widespread clinical application?, Curr. Opin. Biomed. Eng. 10 (2019) 35–44. https://doi.org/10.1016/j.cobme.2019.02.003.

[54] M.P.R. Fernández, P. Mazón, S.A. Gehrke, J.L. Calvo-Guirado, P.N. De Aza, Comparison of two xenograft materials used in sinus lift procedures: Material characterization and in vivo behavior, Materials (Basel). 10 (2017). https://doi.org/10.3390/ma10060623.

[55] F. Riachi, N. Naaman, C. Tabarani, N. Aboelsaad, M.N. Aboushelib, A. Berberi, Z. Salameh, Influence of Material Properties on Rate of Resorption of Two Bone Graft Materials after Sinus Lift Using Radiographic Assessment, Int. J. Dent. (2012) 1–7.

https://doi.org/10.1155/2012/737262.

[56] S. Ma, Y. Yang, D.L. Carnes, K. Kim, S. Park, S.H. Oh, J.L. Ong, Effects of Dissolved Calcium and Phosphorous on Osteoblast Responses, J. Oral Implantol. 31 (2005) 61–67. https://doi.org/10.1563/0-742.1.

[57] J. Xiong, Y. Li, P.D. Hodgson, C. Wen, In vitro osteoblast-like cell proliferation on nano-hydroxyapatite coatings with different morphologies on a titanium-niobium shape memory alloy, J. Biomed. Mater. Res. - Part A. 95 (2010) 766–773. https://doi.org/10.1002/jbm.a.32903.

[58] Z. Shi, X. Huang, Y. Cai, R. Tang, D. Yang, Size effect of hydroxyapatite nanoparticles on proliferation and apoptosis of osteoblast-like cells, Acta Biomater. 5 (2009) 338–345. https://doi.org/10.1016/j.actbio.2008.07.023.

[59] C.Y. Yang, T.M. Lee, C.W. Yang, L.R. Chen, M.C. Wu, T.S. Lui, In vitro and in vivo biological responses of plasma-sprayed hydroxyapatite coatings with posthydrothermal treatment, J. Biomed. Mater. Res. - Part A. 83 (2007) 263–271. https://doi.org/10.1002/jbm.a.31246.

[60] E. Park, R.A. Condrate, D. Lee, Infrared spectral investigation of plasma spray coated hydroxyapatite, Mater. Lett. 36 (1998) 38–43. https://doi.org/10.1016/S0167-577X(97)00287-5.

[61] S. Koutsopoulos, Synthesis and characterization of hydroxyapatite crystals: A review study on the analytical methods, J. Biomed. Mater. Res. 62 (2002) 600–612. https://doi.org/10.1002/jbm.10280.

[62] H. El Feki, C. Rey, M. Vignoles, Carbonate ions in apatites: Infrared investigations in the v4

CO3 domain, Calcif. Tissue Int. 49 (1991) 269–274. https://doi.org/10.1007/BF02556216.

[63] H. Chihi, I. Khattech, M. Jemal, Preparation, characterization and thermochemistry of magnesium carbonate co-substituted fluorapatites, J. Therm. Anal. Calorim. 127 (2017) 2427–2438. https://doi.org/10.1007/s10973-016-5693-2.

[64] K. Anselme, P. Sharrock, P. Hardouin, M. Dard, In vitro growth of human adult bone-derived cells on hydroxyapatite plasma-sprayed coatings, J. Biomed. Mater. Res. 34 (1997) 247–259. https://doi.org/10.1002/(SICI)1097-4636(199702)34:2<247::AID-JBM14>3.0.CO;2-F.

[65] A. John, H.K. Varma, T. V. Kumari, Surface Reactivity of Calcium Phosphate Based Ceramics in a Cell Culture System, J. Biomater. Appl. 18 (2003) 63–78. https://doi.org/10.1177/0885328203018001006.

Electrostatic Spray Deposition

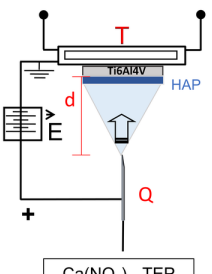

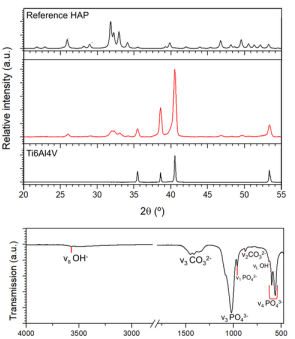

HAP microstructural tuning as function of processing parameter

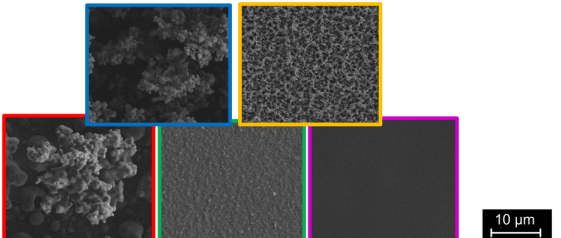

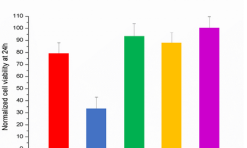

Cell viability test of MG-63 osteoblast like cell on selected HAP coatings